Transport of charge carriers across the normal-superconducting interfaces in $Bi_{1.65}Pb_{0.35}Sr_2Ca_2Cu_3O_{10+\delta}$ nanoceramics

E. Govea-Alcaide [a,b,*], J. Rodríguez-Milanés [b], F. Guerrero [a], C.D. Maasch [c], M.S. Torikachvili [c], R.F. Jardim [d]

[a] *Departamento de Física, Universidade Federal Do Amazonas, Manaus, AM, Brazil*
[b] *Universidad de Granma, Granma, Bayamo, Cuba*
[c] *Department of Physics, San Diego State University, San Diego, CA, 92182-1233, USA*
[d] *Instituto de Física, Universidade de São Paulo, Rua Do Matão, 1371, 05508-090, São Paulo, SP, Brazil*

ARTICLE INFO

ABSTRACT

Samples of superconducting $Bi_{1.65}Pb_{0.35}Sr_2Ca_2 Cu_3O_{10+\delta}$ (Bi-2223) with nanoparticle-sized grains were produced with the help of high-energy ball milling, followed by pelletizing, and flash sintering. X-ray powder diffraction patterns suggest that the grain size was not altered by flash sintering. The temperature dependence of the magnetic susceptibility $\chi(T)$, electrical resistivity $\rho(T)$, and thermoelectric potential $S(T)$, all revealed features consistent with superconductivity below $T_c \approx 108$ K, though these features were progressively suppressed with the milling time. These data indicate that milling generates nanoparticle-sized grains with the Bi-2223 phase at the core, surrounded by a severely damaged and disordered outer shell. The thickness of this outer layer increases with milling time. The extent of the damage surrounding the grain cores has severe implications on the properties of the pellets. While the onset of superconductivity is clearly marked by the diamagnetic response in $\chi(T)$, and a drop in $S(T)$, the signature in $\rho(T)$ is more subtle and difficult to resolve, as it is superimposed on a semiconducting-like resistivity background. Measurements of the real (ε') and imaginary (ε'') components of the dielectric permittivity in the low frequency limit reveal two distinct interfaces of charge accumulation, one at the margins between the crystalline grain cores and the damaged outer layers, and the second between the grain boundaries. The behaviors of $\rho(T)$ and ε'' near room temperature follow closely an Arrhenius dependence, yielding activation energies in the range between 50 and 200 meV. The transport properties can be explained by a hopping model.

1. Introduction

Since the pioneering studies of Ralph, Black, and Tinkham [1,2], a great number of experimental studies of superconductivity in the nanosize particle limit were carried out. This concerns grains in which at least one dimension is ≤ 100 nm. For nanoparticles of superconducting materials, such studies were focused mostly on elemental, type I superconductors (Al, Pb, and Sn), and they mainly probed the magnetic properties [2–5]. Meanwhile, much of the research on nanosized superconducting cuprates have been conducted in superconducting $YBa_2Cu_3O_{7-x}$ [6,7].

More recently, we carried out a systematic study of the magnetic properties of $(Bi,Pb)_2Sr_2Ca_2Cu_{10+y}$ (Bi-2223) nanopowders obtained by means of high-energy ball milling [8]. The average grain size is reduced

with the milling time, and the morphology of the outer layers of the grains changes drastically. While a reduced core of undamaged material remains intact for milling times as long as 210 min, transmission electron microscopy (TEM) images revealed that the outer layers transformed into a condensed debris of damaged material, mostly in the shape of nanorods, with diameters as low as 20 nm. This modified morphology resulted in significant changes in the magnetic susceptibility, of the powder samples in both the superconducting and the normal states, including a ferromagnetic-like contribution at room temperature [8].

In this work we present a systematic study of the magnetic and electronic transport properties of consolidated pellets of $Bi_{1.65}Pb_{0.35}Sr_2Ca_2 Cu_3O_{10+\delta}$ (Bi-2223) nanoceramics. The experimental work includes measurements of magnetic susceptibility as a function of

temperature $\chi(T)$, electrical resistivity $\rho(T)$, thermoelectric potential $S(T)$, and dielectric permittivity $\varepsilon(T)$.

2. Experimental procedure

The starting materials for obtaining nanoparticles were powders of $Bi_{1.65}Pb_{0.35}Sr_2Ca_2Cu_3O_{10+\delta}$ (Bi-2223) prepared by solid state reaction, as described in Ref. [10]. The resulting powders were ground in air at ambient temperature using a FRITSCH Planetary Ball Mill (Pulverisette 5). The initial coarse-grain mass of the Bi-2223 powder was $M \sim 30$ g. The bowl and grinding spheres (10 and 20 mm diameter) were made of tungsten carbide, and the angular velocity $\omega = 200$ rpm [8]. Small samples of ~ 1.5 g were removed at the milling times of $t_m = 0$, 120, 135, 150, 165, and 175 min, to be consolidated into pellets and studied. The pellets of 2 mm thickness were compacted under uniaxially pressures of 500 MPa, and rapidly sintered in air at 750 °C for 30 min. These samples will be hereafter referred to as P0 (reference), P120, P135, P150, P165, and P175, respectively.

X-ray powder diffraction (XRD) scans of powder and pellet samples were carried out in a Bruker-AXS D8 Advance diffractometer. The measurements were performed at room temperature using Cu Kα radiation in the $3° \leq 2\theta \leq 80°$ range with a 0.05° (2θ) step size, and 5 s counting time. Images of grains morphology were collected with a JEOL JSM-5800 Scanning Electron Microscope (SEM) operating at 25 kV.

Magnetization $M(T)$, electrical resistivity, thermoelectric potential, and electrical permittivity measurements were taken in sections of the pelletized samples. The measurements of $\chi(T)$, $M(T)/H$, and $M(T)$ were collected with a SQUID and a vibrating sample magnetometer (VSM) from Quantum Design. Zero-field-cooled (ZFC) and field-cooled (FC) M vs. T curves were used to determine the onset of superconductivity and to estimate the superconducting volume fraction. The measurements of electrical resistivity and magnetoresistance were carried out in rectangular shaped samples using a 4-lead configuration, using the Physical Property Measurement System from Quantum Design, equipped with a 9 T superconducting magnet (PPMS-9). Platinum leads were attached to the samples using Ag-loaded epoxy or Ag-paste. The thermoelectric potential was determined using Quantum Design's thermal transport option, employing a 4 lead configuration as well.

The real ε' and imaginary ε'' components of the dielectric permittivity in the 15–500 K temperature range for frequencies between 200 Hz and 10 MHz, were measured using an Agilent 4284A precision LCR meter. These measurements were performed in a closed cycle cryogenics refrigerator (ARS-4HW/DE-202 N), and the temperature was controlled with a Lakeshore 331S unit.

3. Experimental results and discussion

3.1. X-ray diffraction and morphology

The X-ray powder diffraction (XRD) patterns of the pre-reacted powder, which served as a reference, and samples P0, P120, P150, and P175 are shown in Fig. 1. The $\Theta - 2\Theta$ scans of the reference powder, as well as the P0 sample, display all expected reflections consistent with the high-T_c Bi-2223 phase, indicating a high degree of crystallinity. A calculation of the lattice parameters, assuming an orthorhombic unit cell yields $a = 5.411$ Å, $b = 5.412$ Å, and $c = 37.150$ Å are in line with values obtained in previous studies [10]. The increase in background, and the broadening of the reflections for samples P120, P150, and P175 are consistent with the reduction of the grain sizes upon milling. These changes also suggest a progressive damage of the outer bounds of the grains as a function of the milling time, as already reported elsewhere [8].

It is important to notice that the most prominent Bragg peaks identified in the reference and P0 samples are still discernible in the XRD patterns of samples P120, P150, and P175, thought they all broadened to a large extent. The lower T_c Bi-2212 phase could not identified within
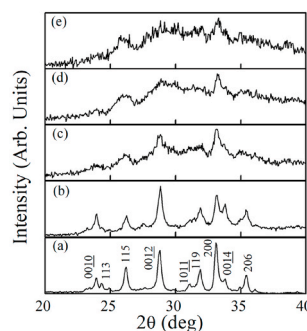

Fig. 1. X-ray diffraction patterns of the pre-reacted powders (a), and powders of pellets P0 (b), P120 (c), P150 (d), and P175 (e). The Bragg reflections belonging to the Bi-2223 phase are identified with Miller indexes in (a).

the resolution of the XRD scans of Fig. 1, neither in the reference sample, nor in the milled powders or sintered pellets. However its presence cannot be completely ruled out, given that it frequently accompanies the formation of the Bi-2223 phase, and some interplanar distances are close.

SEM images of the samples P0, P150, and P175 are shown in Fig. 2. These images show that all samples have a broad distribution of particle size and different morphologies. The P0 sample of Fig. 2 (a) exhibits platelet-like grains with typical lengths of ≈ 2 μm. This platelet-like morphology is typical of Bi-2223 superconducting grains [9]. Debris of damaged material form around the platelets upon milling, and their typical lengths drop to < 1 μm, as seen in Fig. 2(b) and (c) for P150 and P175, respectively.

3.2. Magnetization as a function of temperature

ZFC measurements of $\chi(T)$ at H = 10 Oe are displayed in Fig. 3, and they clearly show the onset of diamagnetism near $T_c \approx 108$ K for all samples, though the signal level decreased with milling time. The values of T_c are in excellent agreement with values found for single-phase Bi-2223 [10]. The drop in the magnitude of the diamagnetic signal with milling time is suggestive that only a smaller portion of each grain remained superconducting. This loss of superconducting volume suggests that by impinging severe damage to the outer layers of the grains, the damaged material loses its SC, while the grain cores that remained unaffected by the milling retained their ability to superconduct. The increased damage to the outer layers of the grains as a function of the milling time, which is consistent with the broadening of the X-ray reflections, is consistent with the metallography as well. The $\chi(T)$ data of Fig. 3 show also that the paramagnetic component below 20 K becomes more discernible for the samples milled longer. A broad bump centered near 70 K is possibly due to the superconductivity of a trace amount of Bi-2212 minority phase.

Detailed measurements of ZFC and FC $\chi(T)$ for P120 and P150 in H = 10 Oe are shown in Fig. 4. Both samples show clear onset of superconductivity near 108 K, as well as upturns in $\chi(T)$ of similar magnitude at low temperatures. The upturn can be seen more prominently in the P150, which was milled longer and therefore has a lower diamagnetic signal below T_c. This drop in superconducting volume with milling time is consistent with the behavior observed in the nanopowders used in the sintered pellets [8], and with the loss of crystallinity of the outer layers as suggested by the XRD analysis.

It is noteworthy to point out that the behavior of $\chi(T)$ below T_c for the consolidated pellets and the pre-reacted milled powders is about the same, and consistent with the change of the grain morphology upon milling [8]. The similar behaviors of the original powders and sintered pellets suggest that the pellets are composed of grains with undamaged cores surrounded by layers of damaged and disordered material.

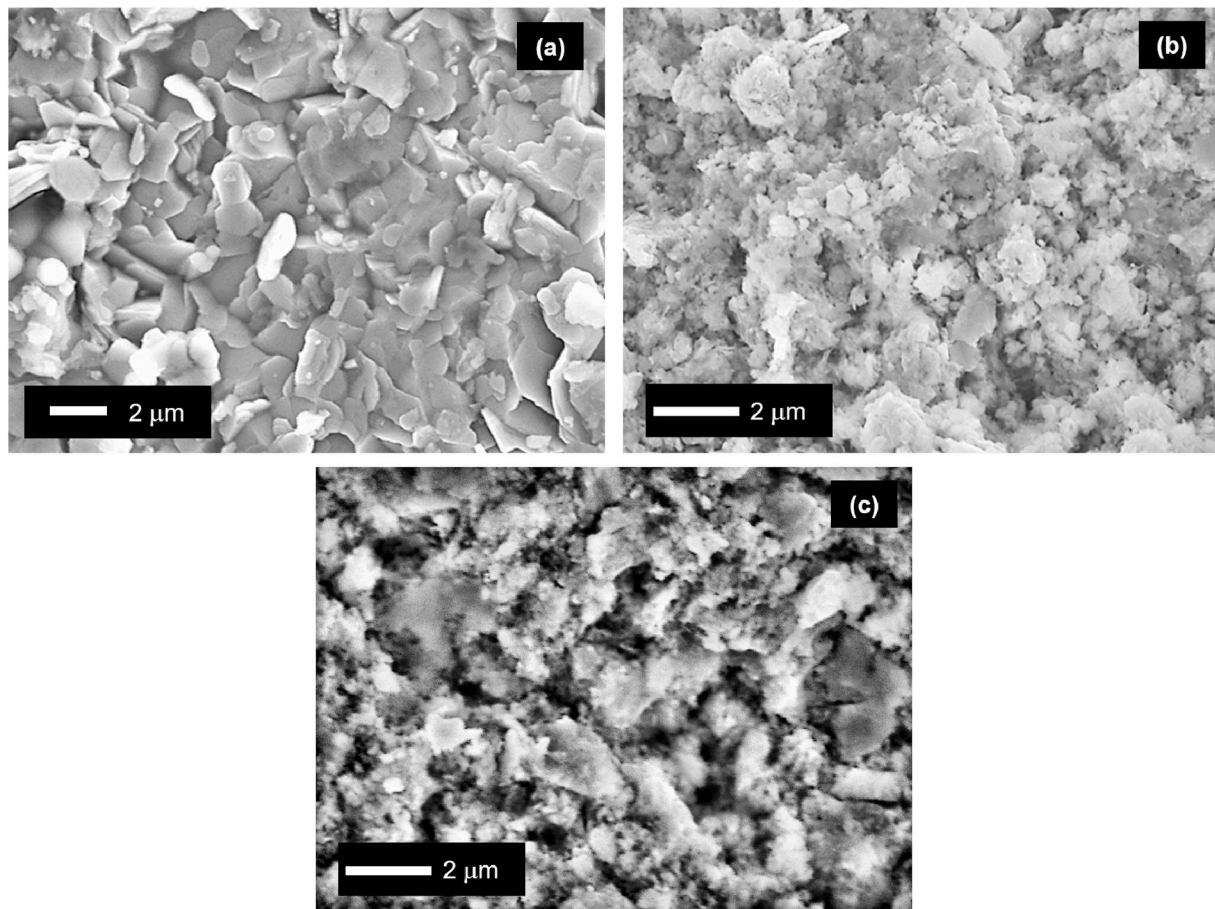In order to further probe the changes of the superconducting state

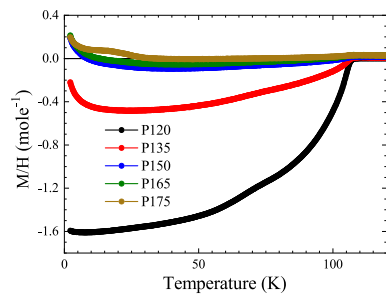**Fig. 2.** SEM images of samples: (a) P0, (b) P150, and (c) P175.

Fig. 3. ZFC $\chi(T)$ at 10 Oe for all Bi-2223 pellet samples of this work. The onset of superconductivity near $T_c \approx 108$ K can be clearly seen, thought zooming is required for the samples milled longer.

upon milling, as revealed in the $\chi(T)$ data, we carried out measurements of electrical resistivity, thermoelectric potential, and electric permittivity.

3.3. Electrical resistivity

The temperature dependence of the electrical resistivity for samples P120, P135, and P150 is shown on Fig. 5. Given the extensive damage around the Bi-2223 cores, the percolation is compromised, the overall behavior of $\rho(T)$ is semiconductor-like, and the negative value of the temperature dependence coefficient scales with the milling time. While for the P120 sample the resistance at low temperatures was low enough that it could be measured reliably, the resistance of the P135 and P150 samples started becoming prohibitively high and could not be precisely
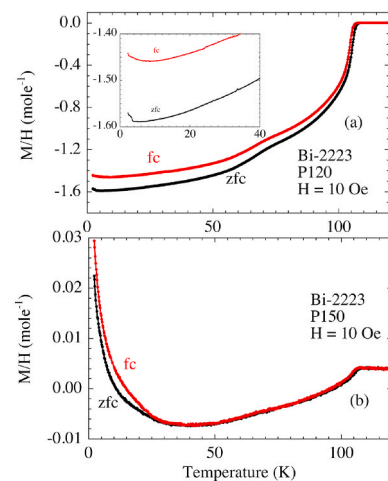

Fig. 4. ZFC and FC $\chi(T)$ at 10 Oe for samples P120 (a) and P150 (b). The value of $T_c \approx 108$ K is the same for both samples. The magnitude of the diamagnetic signal corresponding to SC is about two orders of magnitude higher for P120 than P150, reflecting the extensive damage to the outer layers of the Bi-2223 grains in the latter.

determined.

Displayed in Fig. 6 is a plot of $\rho(T)$ for the P120 sample in H = 0 and 9 T, with the corresponding derivatives $d\rho/dT$ in the inset. There is a noticeable change in inflection of $\rho(T)$ near T_c, which corresponds to an anomaly in the derivative for H = 0. This anomaly gets washed off in a 9 T field. The upturn in resistivity below T_c is reminiscent of the behavior
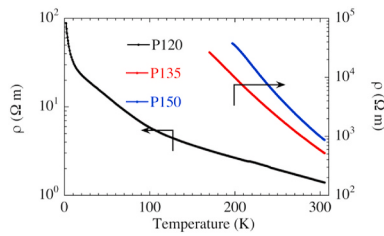
Fig. 5. Electrical resistivity vs temperature for P120, P135, and P150.
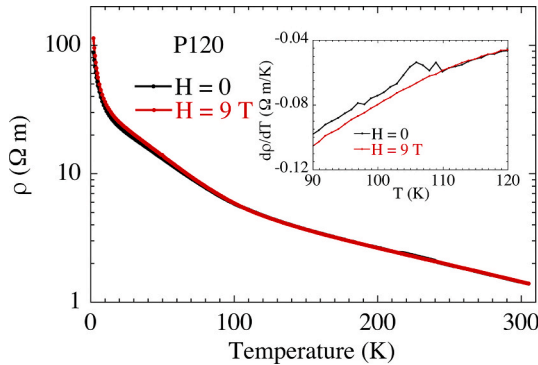

Fig. 6. Electrical resistivity vs temperature for P120 in H = 0 and 9 T. The upturn in $\rho(T)$ near T_c and the slightly higher values of resistivity below T_c in H = 9 T are consistent with superconducting grain cores being surrounded by non-superconducting outer layers.

in granular superconductors (e.g. $Sm_{1.83}Ce_{0.17}CuO_{4-y}$) (Ref. [11]), which has been addressed with the two-fluid model, i.e., a metallic-insulating two-phase mixture [12]. In essence, the superconducting condensation at T_c starves the single carrier tunneling from the Bi-2223 cores to the outer semiconducting interfaces, leading to an upturn in $\rho(T)$ below T_c [11,12]. The anomaly in $\rho(T)$ near T_c, and the consistent higher values of $\rho(T)$ for H = 9 T, are compatible with superconductivity taking place in the core of the grains, even though the more typical behavior of $\rho(T)$ for superconductors is being masked by the dominant semiconductor-like behavior of the outer layers of the grains.

In light of the semiconducting behavior being predominantly determined by the damaged outer layers of the grains, an estimate of the activation energy E_a for the resistivity can be extracted assuming an Arrhenius law expression $\rho(T) = \rho_{300K}\exp(-E_a/k_BT)$, where k_B is the Boltzmann constant. The values of E_a can be estimated from the slopes of $\ln(\rho(T)/\rho_{300K})$ vs $1/T$ near 300 K, as shown in Fig. 7, yielding $\approx$ 47, 184, and 217 meV, respectively, for P120, P135, and P150.
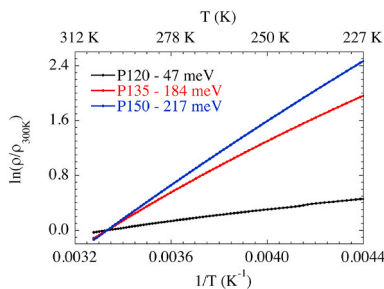

Fig. 7. $\ln(\rho/\rho_{300K})$ vs $1/T$ for P120, P135, and P150. The values of E_a were extracted from the slopes near 300 K.

3.4. Thermoelectric potential (TEP)

The resistivity of the P120 sample is low enough that it permitted measurement of the TEP down to and below T_c. Shown in Fig. 8(a) is the temperature dependence $S(T)$ in magnetic fields from 0 to 9 T. The sharp drop from $\approx$ 12 μV/K towards zero centered near 104 K is due to the onset of superconductivity. It is quite plausible that the second step starting and below $\approx$ 95 K is due to the presence of some 2212 phase. The effect of the magnetic field is to shift T_c to lower temperatures, consistently with an increase of the upper critical magnetic field H_{c2} upon cooling down from T_c. The drop in TEP at T_c, in spite of the high overall resistance of the sample, gives credence to the notion that the ball milled grains are made of superconducting cores surrounded by severely damaged outer layers. Although the outer layers impose a high but finite overall resistance on the sample, if the grain cores are superconducting, the $V = 0$ state from the cores *leaks out* to the whole grains, leading to an overall TEP = 0 below T_c. The values of H_{c2} extracted from the transition midpoints of the TEP are shown in Fig. 8(b).

The values of H_{c2} from Fig. 8(b) can be used to estimate $H_{c2}(0)$ and the coherence length (ξ). A rough estimate of $H_{c2}(0)$ for superconductivity in the dirty limit can be made using the expression proposed by Werthamer, Helfand, and Hohemberg (WHH) [13].

$$H_{c2}(0) = -0.693\, T_c\, (dH_{c2}/dT)|_{T_c}. \tag{1}$$

Using $T_c = 103.6$ K and $dH_{c2}/dT|_{T_c} = 0.07$ T/K, we obtained $H_{c2}(0) = 5$ T. Given the upturn of H_{c2} vs T of Fig. 8(b), and the large anisotropy of the Bi-2223 compounds, this H_{c2} value is most likely the upper limit for H||c, i.e. $H_{c2,c}(0) = 5$ T. The data of Fig. 8(b), albeit limited to a 9 T field, could be also fit and extrapolated to $T = 0$ using the phenomenological expression [14].

$$H_{c2}(T) = H_{c2}(0)\left[1 - (T/T_c)^2\right]^\alpha \tag{2}$$

The good fit displayed in Fig. 8(b) was obtained with $H_{c2}(0) = 35$ T,
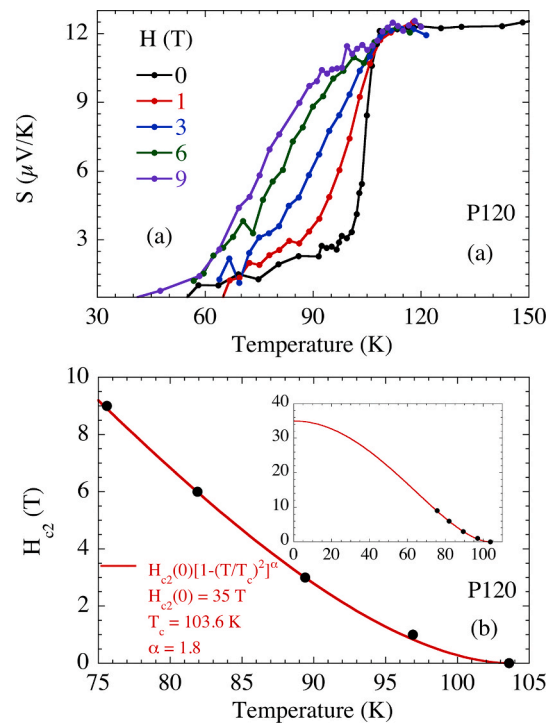

Fig. 8. (a) Thermoelectric potential vs temperature for the P120 sample in the range $H = 0$ to 9 T. (b) H_{c2} vs T extracted from the midpoint of the superconducting transitions in the TEP data. The solid line is a fit of $H_{c2}(T)$ to a phenomenological expression.

and $\alpha = 1.8$. Clearly this H_{c2} value represents $H_{c2,ab}(0)$. The ratio $\gamma = H_{c2,ab}(0)/H_{c2,c}(0) = 6.4$ is within a reasonable range for Bi-2223 compounds, given the uncertain level of the misorientation of the grains in our samples. In light of the Ginzburg-Landau expression correlating H_{c2} with ξ [14].

$$H_{c2}(0) = \varphi_0 / \left(2\,\pi\,\xi_0^2 \right), \tag{3}$$

where $\varphi_0 = 2.068 \times 10^{-15} T/m^2$ (magnetic flux quantum). Given that and $\xi(0)$ in anisotropic systems correspond to orthogonal directions, the values for $\xi_{ab}(0)$ and $\xi_c(0)$ turn out to be 31 and 81 Å, respectively. These values are similar to those reported previously for the same compound [15].

3.5. Dielectric properties

In light of the overall semiconductor-like behavior of the electronic transport properties of the ball milled samples, resulting from the convolution of conducting grain cores and poorly conducting outer layers, measurements of dielectric response as a function of temperature are in order. Shown in Fig. 9 are the behaviors of ε' and ε'' as a function of temperature for the five ball milled samples of this study. The typical behavior is an almost flat dependence of ε' and ε'' with temperature up to ≈ 65 K (P120, and P135), or ≈ 140 K (P150, P165, and P175), followed by gradual upturns to higher values, increasing between 1 and 2 orders of magnitudes by 300 K. The inset of Fig. 9(b) shows an almost linear drop of the $T = 0$ extrapolated values of ε'' with milling time. Similar overall behavior was also reported for ceramic pellets of $YBa_2Cu_3O_{6+x}$ ($x \approx 0$) [16] and $Bi_{4-n}Pb_nSr_3Ca_3Cu_4O_x$ ($0 \leq n \leq 1$) glasses [17,18].

The values of ε' and ε'' at low temperatures are low and nearly independent of temperature, suggesting a regime dominated by frozen polarons, reminiscent of $CaCu_3Ti_4O_12$[20]] Focusing on P120 sample for the sake of this argument, a tangible increase in permittivity can be observed in the 65–150 K, which is likely related to the excitation of polarons within the grains. These polarons start to move within the grains due to the applied electric field and are trapped primarily at grain boundaries, resulting in a net polarization of the system and a

corresponding increase of the permittivity. The permittivity starts to rise more rapidly above ≈ 150 K, which can be attributed possibly to the thermal activation conductivity inside the cores. While these two different regimes overlap and are convoluted in the P120 sample, they are more clearly separated for the P135 sample, as suggested by the behavior of ε'' in Fig. 9(b). While the frozen polaron and thermally activated regimes overlap in samples P120 and P135, the two mechanisms extend over a broader temperature range for samples P150, P165, and P175. In the latter, the temperature range dominated by frozen polarons stretches up to higher temperatures (≈ 140 K), followed by the excitation of intergranular polarons becoming more relevant near 200 K. For temperatures higher than ≈ 200 K, a third domain in temperature takes over, where the thermally activated conductivity or hopping of charge carriers start to become more relevant.

Given the presence of two interfaces in the ball-milled samples, core-outer shell and outer shell – outer shell, an analysis of the dielectric loss as a function of temperature and frequency is in order. The temperature dependence of the dielectric loss $\tan \delta = (\varepsilon''/\varepsilon')$ for samples P120 and P165 are shown in Fig. 10 (a) and (b), respectively. These data show two distinct temperature regions that can be linked to two different mechanisms. First, a Debye-like peak is progressively shifted to higher temperatures with frequency, and secondly, the loss increases rapidly at higher temperatures. The latter is easier to see for low frequencies, getting out of the temperature range of Fig. 10 for higher frequencies. These two regions start to overlap in samples with longer milling times, since the Debye-like peaks are shifted to higher temperatures and dielectric losses increase.

Given the high temperatures required to sinter ceramic materials, oxygen deficiency is quite frequent, and oxygen vacancies can be linked to the reduction of chemical elements with high oxidation states [21–23]. Since the charge carriers in the Bi-2223 are located on the Cu–O planes, Cu is the ion responsible for the short-range hopping in these samples.

It is well established that the complex dielectric permittivity ε of a given material is mainly determined by the superposition of three contributions: (i) the electronic, related to the displacement of the electronic charge distribution relative to their nuclei; (ii) the lattice, associated with the displacement of ions and their charge distributions; and (iii) the dipolar polarization, associated with permanent dipoles or dipolar effect related to impurities, lattice defects, or charge carriers (electrons, holes, or ions) [16,19]. These contributions are also known for having different frequency responses. For instance, while at low
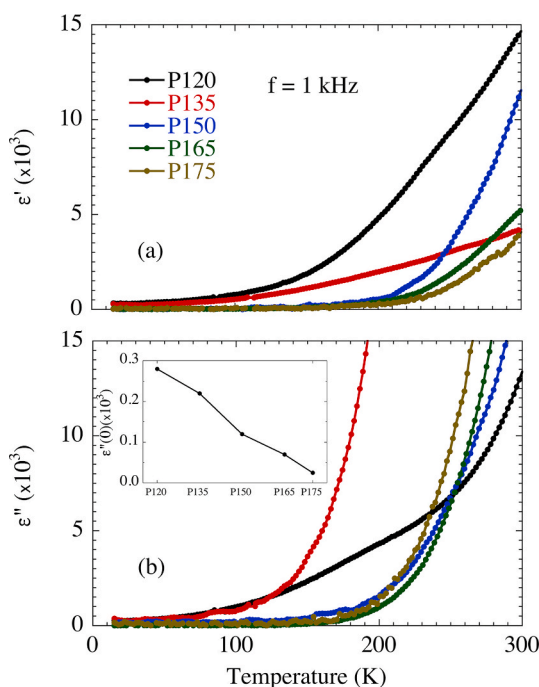

Fig. 9. Temperature dependence of ε' (a) and ε'' (b) for samples P120, P135 P150, P165, and P175 measured at f = 1 kHz. The inset in (b) is the complex permittivity extrapolated to T = 0 K for each studied sample.
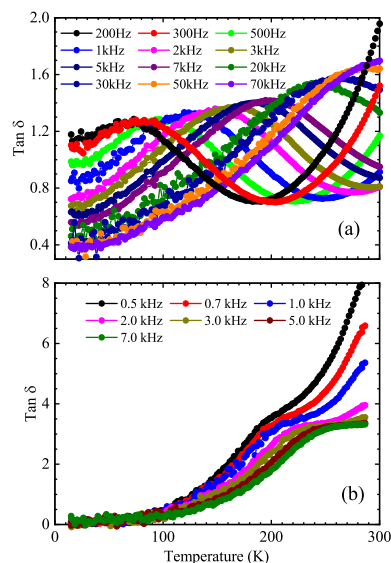

Fig. 10. Dielectric loss measured at different frequencies in samples P120 (a) and P165 (b). Lines between points are guides for eyes.

frequencies all contributions are present, at higher frequencies the dipolar polarization stemming from lattice defects or charge carriers can be disregarded [16,19]. By taking these points into consideration, we focused in the behavior in the low frequency regime (f = 1 kHz), and the data is displayed in Fig. 9. The first point to be addressed is the abrupt increase in $\varepsilon''(T)$, a feature certainly related to dipolar effects [16,19]. It is important to notice that in these oxides, hopping of charge carriers occurs by electronic or ion (oxygen) transport mechanisms, the latter being expected to occur at temperatures well above room temperature. Thus, by virtue of the performed measurements at f = 1 kHz, hopping of charge carriers seems to be the dominant mechanism for the dielectric loss in these pellet samples.

Fig. 11(a) displays the $\log \varepsilon''(T)$ vs. 1000/T plot for all samples. The ε'' curves show linear behavior at high temperatures, $200 \le T \le 300$ K, obeying the Arrhenius law. However, such behavior is only observed for temperatures higher than 260 and 230 K in samples P120 and P135, respectively. The activation energy extracted from the transport process, E_a, was then determined from the linear fit of the dielectric loss data to the equation $\varepsilon''(T) \propto \exp(E_a/(k_B T))$, where k_B is the Boltzmann constant. Values of E_a extracted from all pellet samples are displayed in Fig. 11(b) and the show that the activation energy rises appreciably from sample P125 to P165, from ~ 0.12 to ~ 0.20, after which it drops slightly for sample P175. These E_a values are of the same order of magnitude of those reported for superconducting cuprates, and therefore lend credence to the notion of carrier hopping being the dominant process for electrical conductivity in our samples [16–18].

The dipolar conductivity σ is related to the dielectric loss by the relationship $\sigma = (\omega \varepsilon_0 \varepsilon'')/4\pi$, where $\omega = 2\pi f$ is the angular frequency and ε_0 is the permittivity of vacuum. It is then plausible to assume that charge carriers start to accumulate near the core-shell interfaces with increasing temperature. In fact, for $T < 200$ K, the concentration of carriers accumulated along the core-shell interfaces is expected to be low and σ assumes very low values (~ 0). As the temperature increases above ~ 200 K, the accumulation of carriers near the interfaces increases as well as the dipolar conductivity. Also, for temperatures high enough ($T > 200$ K), a portion of carriers overcomes the interface of the shell barrier and hopping of carrier is established. This process continues and accumulation of carriers is expected to occur once again but now at grain boundaries between granules of the material. At $T = 300$ K, the maximum temperature of our experiments, the conduction process across grain boundaries is further enhanced. Finally, we emphasize that E_a increases from sample P120 to P165 and it remains close for samples

P165 and P175. This result clearly indicates that more energy is required to trigger the hopping conduction across the shell, and that an increase in the thickness of the disordered outer layer takes place surrounding the grain cores subjected to a prolonged milling time.

In order to gain insight into the electrical conductivity in the damaged outer layers, values of the activation energy E_a were determined from the curves of the dc conductivity σ_{dc} vs inverse temperature using the Arrhenius law, as shown in Fig. 12. Fig. 12 (a) shows the frequency dependence of the conductivity for sample P165, in the temperature range between 200 and 300 K. By taking the slopes of these curves at frequencies varying from 10^2 to 10^6 Hz, we graphed $\ln(\sigma_{dc}T)$ vs 1/T, from which we extracted E_a values using the Arrhenius law. These plots yielded E_a values of 129, 169, 177, 206, and 203 meV for samples P120, P135, P150, P165, and P175, respectively, with errors within 5 %. These values of E_a are in excellent agreement with the values obtained from the plots of $\ln \varepsilon''$ vs 1/T of Fig. 11(b), lending credence to
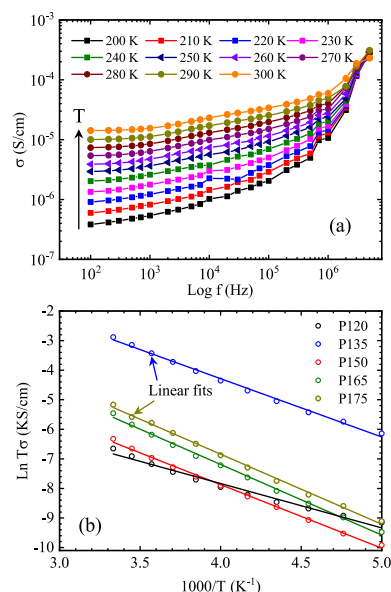
Fig. 12. Frequency dependence of dc conductivity for sample P165 (a). From these experimental curves the Arrhenius plots for all studied samples were obtained and are displayed in (b).
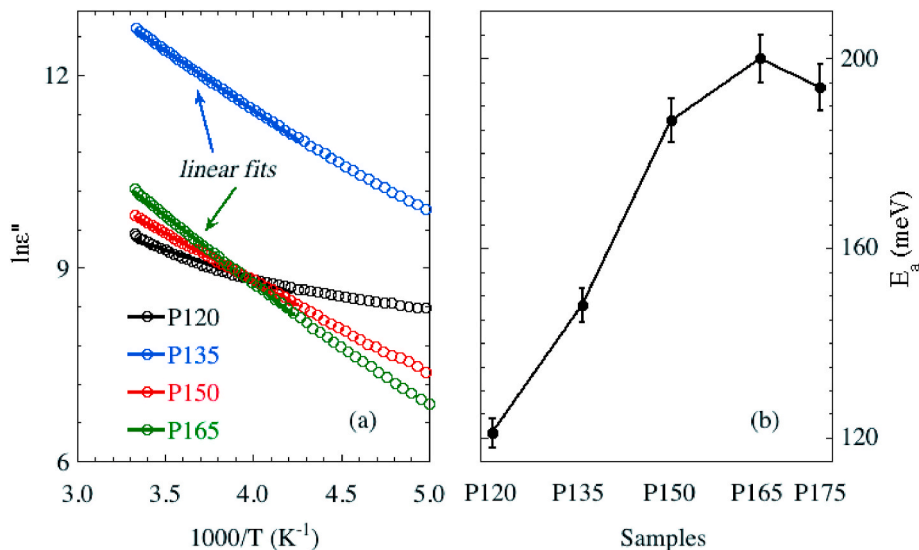
Fig. 11. (a) $\log \varepsilon''(T)$ vs. 1000/T plot for f = 1 kHz and (b) activation energy, E_a, for all studied samples (see text for details). Bars represent the 5 % of the relative error and lines are guide for the eyes.

the notion that the hopping of charge carriers between granules at temperatures higher than 200 K constitutes the main transport mechanism.

4. Conclusions

We carried out a thorough investigation of Bi-2223 superconductors synthesized from single phase powders, after the powder was ball milled thoroughly to attain nanosize dimensions. Powder XRD analysis shows broadening of the reflections and an increase in the background as a function of the milling time, while the SEM images reveal a severe reduction in particle size, and drastic change in morphology. The $\chi(T)$ data show that superconductivity in the samples made from ball milled particles still has a T_c onset ≈ 108 K. However, the superconducting volume drops precipitously with milling time. While the onset of superconductivity is clearly marked by the diamagnetic response in $\chi(T)$, the signature in $\rho(T)$ is more subtle and difficult to detect, as it is superimposed on the semiconducting-like resistivity of the background provided by the damaged outer layers of the grains. A meticulous analysis of the $\rho(T)$ data clearly indicates that superconductivity from the center of the damaged grain can still be detected. In spite of the overall semiconducting behavior of the P120 sample, its resistivity was low enough that measurements of $S(T)$ were possible, and they clearly revealed superconducting transitions consistent with the $\chi(T)$ and $\rho(T)$ data. Actually, the $S(T)$ data in magnetic fields up to 9 T yielded the typical $H_{c2}(T)$ behavior of Bi-2223 materials, from which the values of the anisotropic coherence lengths could be estimated. The measurements of $\varepsilon(T)$ permitted the identification of two interfaces, one from the core of the grains to the damaged outer layers, and another from the intergranular junctions formed upon sintering. It is important to point out that the activation energies obtained from the $\rho(T)$ and $\varepsilon(T)$, which are somewhat apart for the P120 sample (0.05 and 0.12 eV, respectively) start to converge for the longer milled samples, e.g. 0.21 and 0.19 eV for the P150 sample. This convergence should be expected as the size of the metallic core gets reduced. In summary, this set of data builds a picture in which the ball milling process wears out and damages the outer layers of the grains progressively. However, if enough of the grain cores remains undamaged, superconductivity can still be observed.

Declaration of competing interest

The authors declare that they have no known competing financial interests or personal relationships that could have appeared to influence the work reported in this paper.

Acknowledgements

References

[1] D.C. Ralph, C.T. Black, M. Tinkham, Spectroscopic measurements of discrete electronic states in single metal particles, Phys. Rev. Lett. 74 (1995) 3241–3244.

[2] C.T. Black, D.C. Ralph, M. Tinkham, Spectroscopy of the superconducting gap in individual nanometer-scale aluminum particles, Phys. Rev. Lett. 76 (1996) 688–691.

[3] S. Reich, G. Leitus, R. Popovitz-Biro, M. Schechter, Magnetization of small lead particles, Phys. Rev. Lett. 91 (2003) 147001–147005.

[4] S. Bose, P. Raychaudhuri, R. Banerjee, P. Vasa, P. Ayyub, Mechanism of the size dependence of the superconducting transition of nanostructured Nb, Phys. Rev. Lett. 95 (2005) 147003–147007.

[5] W.H. Li, C.W. Wang, C.Y. Li, C.K. Hsu, C.C. Yang, C.M. Wu, Enhancement of superconductivity by the small size effect in in nanoparticles, Phys. Rev. B 77 (2008) 94508–94515.

[6] P. Paturi, J. Raittila, H. Huhtinen, V.P. Huhtala, R. Laiho, Size-dependent properties of YBaCu$_3$O^{6+x} nanopowder, J. Phys. Condens. Matter 15 (2003) 2103–2114.

[7] S.K. Hasanain, N. Akhtar, A. Mumtaz, Particle size dependence of the superconductivity and ferromagnetism in YBCO nanoparticles, J. Nanoparticle Res. 13 (2010) 1953–1960.

[8] E. Govea-Alcaide, L. Pérez-Acosta, P.K. Kiyohara, R.F. Jardim, Diamagnetic, paramagnetic, and ferromagnetic properties of ball milled Bi$^{1.65}$Pb$^{0.35}$Sr^{2}Ca^{2}Cu^{3}O$^{10+\delta}$ powders, J. Nanoparticle Res. 17 (2015) 432–442.

[9] G. Yildirim, M. Dogruer, F. Karaboga, C. Terzioglu, Formation of nucleation centers for vortices in Bi-2223 superconducting core by dispersed Sn nanoparticles, J. Alloys Compd. 584 (2014) 344–351.

[10] E. Govea-Alcaide, I.F. Machado, R.F. Jardim, 10 to 25-fold increase in the transport superconducting critical current density of spark-plasma sintered Bi-2223 superconductors, J. Appl. Phys. 117 (2015), 043903-1-043903-5.

[11] M.J.R. Sandim, P.A. Suzuki, S. Spagna, S.C. Tripp, R.E. Sager, R.F. Jardim, Increased resistance below the superconducting transition in granular Sm$^{1.83}$Ce$^{0.17}$CuO^{4-y} compounds, Physica C 289 (1997) 265–274.

[12] C.J. Adkins, J.M.D. Thomas, M.W. Young, Increased resistance below the superconducting transition in granular metals, J. Phys. C Solid State Phys. 13 (1980) 3427–3438.

[13] N.R. Werthamer, E. Helfand, P.C. Hohemberg, See, for instance, temperature and purity dependence of the superconducting critical field, H$_{c2}$.III. Electron spin and spin-orbit effects, Phys. Rev. 147 (1966) 295–302.

[14] M.T. Escote, V.A. Meza, R.F. Jardim, L. Ben-Dor, M.S. Torikachvili, A.H. Lacerda, Upper critical field of the magnetic superconductor RuGd$^{1.4}$Ce$^{0.6}$Sr^{2}Cu^{2}O^{10-y}, Phys. Rev. B 66 (2002), 144503.

[15] E. Govea-Alcaide, P. Mune, R.F. Jardim, Flux-line-lattice melting and upper critical field of Bi$^{1.65}$Pb$^{0.35}$Sr^{2}Ca^{2}Cu^{3}O$^{10+\delta}$ ceramic samples, J. Supercond. Nov. Magnetism 25 (2012) 779–784.

[16] G.A. Samara, W.F. Hammetter, E.L. Venturini, Temperature and frequency dependences of the dielectric properties of YB^{2}Cu^{3}O6+x (x $\approx$0), Phys. Rev. B 41 (1990) 8974–8990.

[17] K.K. Som, S. Mollah, K. Bose, B.K. Chaudhuri, Debye-type dielectric behavior of Bi-Sr-Ca-Cu-O-based transition-metal oxide glasses: precursors for oxide superconductors, Phys. Rev. B 47 (1993) 534–537.

[18] S. Mollah, S. Chatterjee, S. Chakraborty, B.K. Chaudhuri, Dielectric properties of semiconducting Bi^{4-n}PbnSr^{3}Ca^{3}Cu^{4}Ox (0 = n = 1) glasses: precursors for high-Tc superconductors, Philos. Mag. B 71 (1995) 151–162.

[19] I. Bhat, S. Husain, W. Khan, S.I. Patil, Structural, transport, magnetic, and dielectric properties of La^{1-x}Te$_x$MnO^3 (x = 0.10 and 0.15), J. Mater. Sci. 48 (2013) 3272–3282.

[20] L. Liu, S. Ren, J. Liu, F. Han, J. Zhang, B. Peng, D. Wang, A.A. Bokov, Z.-G. Ye, Localized polarons and conductive charge carriers: understanding CaCu^{3}Ti^{4}O^{12} over a broad temperature range, Phys. Rev. B 99 (2019) 94110–94118.

[21] X. Zheng, S. Wang, J. Wang, W. Hua, J. Zhang, L. Liu, Long-range and short-range transport dynamics of Li ions in LiMn^{2}O^4, J. Phys. Chem. C 124 (2020) 25254–25261.

[22] L. Liu, D. Shi, S. Zheng, Y. Huang, S. Wu, Y. Li, L. Fang, C. Hu, Polaron relaxation and non-ohmic behavior in CaCu^{3}Ti^{4}O^{12} ceramics with different cooling methods, Mater. Chem. Phys. 139 (2013) 844–850.

[23] S. Ren, J. Liu, D. Wang, J. Zhang, X. Ma, M. Knapp, L. Liu, H. Ehrenberg, Dielectric relaxation behavior induced by lithium migration in Li$_4$Ti^{5}O^{12} spinel, J. Alloys Compd. 793 (2019) 678–685.